Nanoscale Advances

PAPER

View Article Online
View Journal | View Issue



Cite this: *Nanoscale Adv.*, 2019, **1**, 2598

# Formation of strong $L1_0$-FePd/α-Fe nanocomposite magnets by visualizing efficient exchange coupling†

Kenshi Matsumoto,[a] Ryota Sato,[b] Thang Thuy Trinh,[b] Noritsugu Sakuma,[c] Tetsuya Shoji,[d] Mitsutaka Haruta,[b] Hiroki Kurata[b] and Toshiharu Teranishi *[b]

Received 9th April 2019
Accepted 20th May 2019

DOI: 10.1039/c9na00225a

rsc.li/nanoscale-advances

Conceptual nanocomposite magnets (NCMs) composed of exchange-coupled hard/soft magnetic phases have been expected to show excellent magnetic performance based on simultaneous high coercivity ($H_c$) and high saturation magnetization ($M_s$). In our previous works, however, the $H_c$ was considerably lower than its theoretical value ($H_a$), which prevented us from improving the performance of NCMs. Here, we show that the $H_c$ of isolated particulate $L1_0$-FePd/α-Fe NCMs is dominated by their phase segregation into core/shell-like structures *versus* Janus-like structures. Using first-order reversal curve (FORC) analysis, we clearly distinguished a microscopically undetectable difference in the phase-segregation structure in the NCMs, finding both efficient and inefficient exchange coupling. The nanostructurally controlled NCMs dominated by core/shell-like structure with efficient exchange coupling showed the largest energy product ($(BH)_{max}$ = 17.5 MGOe) in the Fe–Pd system and the highest $H_c/H_a$ value (26.5%) among all NCM powders.



## Introduction

Electric energy is mostly consumed by conversion into mechanical energy, where permanent magnets play an important role. Thus, highly efficient conversion of electric energy into mechanical energy depends on high-performance permanent magnets that have both high coercivity ($H_c$) and high saturation magnetization ($M_s$). Exchange-coupled nanocomposite permanent magnets (NCMs) composed of magnetically hard and soft phases have been theoretically expected to show higher performance than the neodymium magnets.[1–3] To bring out their full potential, NCMs should have soft magnetic phases within the nanoscale exchange-coupling length so they can derive a high $M_s$ and $H_c$ from their soft and hard phases, respectively.[3] In many previous works, NCMs were synthesized at the necessary conditions for high performance, but their $H_c$ was much lower than the anisotropy field ($H_a$), which is the $H_c$ upper limit.[4–7] Thus, to improve the $H_c$ of NCMs, we must clarify what determines their $H_c$.

In single-phase magnets, $H_c$ is influenced by many factors such as magnetic-domain interaction,[8] crystal structure,[9] magnetic-domain size[10] and magnetic-domain shape.[10,11] The $H_c$ of NCMs, however, may be influenced by not only these factors but also the interface-inducing lattice strain between the soft/hard phases,[4] the volume ratio[4,12] and the phase-segregation structure[12] of the soft/hard magnetic phases. However, the thermal annealing done at high temperatures to induce atomic diffusion, often necessary to form NCMs, makes it much more difficult to control the nanostructures of NCMs.[4,6,12] Because these several factors are intertwined complexly, improving $H_c$ systematically in various NCMs has been very challenging.

To find the dominant factor determining the $H_c$ of NCMs, we must systematically control several factors that vary $H_c$. We selected $L1_0$-FePd as the hard magnetic phase and α-Fe as the soft magnetic phase, because α-Fe can coexist with $L1_0$-FePd, according to the Fe–Pd phase diagram.[13] Moreover, we can easily control nanostructures such as the crystalline size of the $L1_0$-FePd phase corresponding to the magnetic-domain size under the single domain size (<330 nm), the hard/soft phase volume ratio and the magnetic-domain shape of the NCMs by the reduction–diffusion method (Fig. 1a and Table S1†).[4,5] Furthermore, we visualized the $H_c$ change of NCMs with various nanostructures by using first-order reversal curves (FORCs) analysis, which is a powerful way to confirm the formation of NCMs.[2,4,14,15] This analysis can sensitively distinguish the

[a]*Department of Chemistry, Graduate School of Science, Kyoto University, Gokasho, Uji, Kyoto 611-0011, Japan*

[b]*Institute for Chemical Research, Kyoto University, Gokasho, Uji, Kyoto 611-0011, Japan. E-mail: teranisi@scl.kyoto-u.ac.jp*

[c]*Higashifuji Technical Center, Toyota Motor Corporation, 1200 Mishuku, Susono, Shizuoka 410-1193, Japan*

[d]*Technology Research Association of Magnetic Materials for High-Efficiency Motors (MagHEM), Higashifuji Branch, 1200 Mishuku, Susono, Shizuoka 410-1193, Japan*

† Electronic supplementary information (ESI) available: Experimental details on the synthesis and the material and magnetic characterization of NCMs with different size and compositions. See DOI: 10.1039/c9na00225a

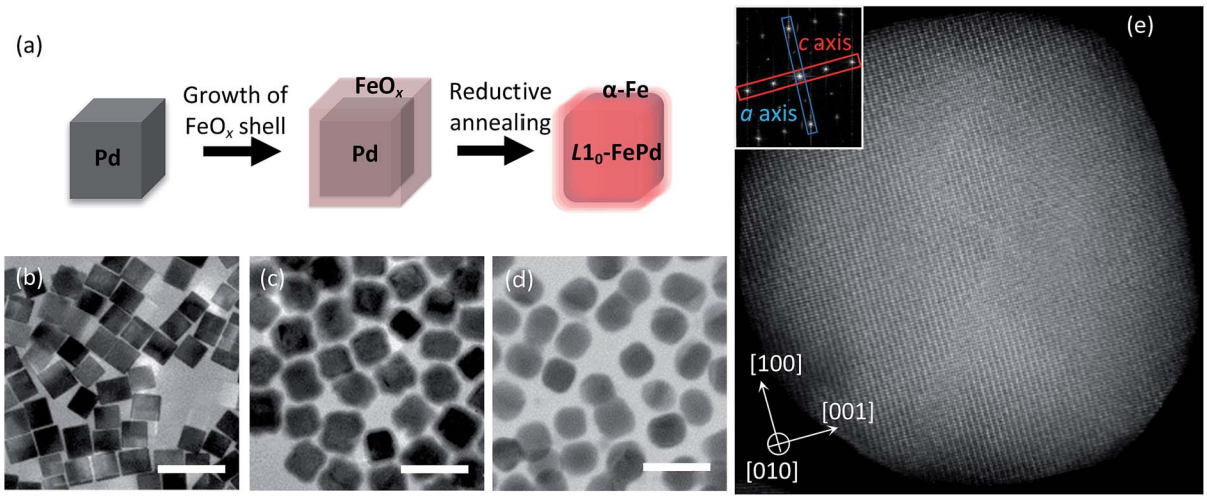


Fig. 1 (a) Synthesis of an $L1_0$-FePd/α-Fe NCM with a well-controlled nanostructure. (b–d) TEM images of (b) 19 nm Pd NCs, (c) Pd@$FeO_x$ NCs with Fe/Pd = 66/34 at% and (d) $L1_0$-FePd/α-Fe NCMs synthesized under reductive annealing of (c) at 560 °C for 3 h. Scale bars are 50 nm. (e) High-angle annular dark-field scanning TEM (HAADF-STEM) image of (d) showing the $L1_0$ structure in the $L1_0$-FePd phase. The inset in (e) shows the fast Fourier transform (FFT) image, in which the spots surrounded by blue and red rectangles respectively imply the planes of the *a* axis and *c* axis of the $L1_0$ structure.

magnetic circumstances affecting $H_c$, letting us quantitatively evaluate the hard/soft exchange coupling of well-defined $L1_0$-FePd/α-Fe NCMs (Fig. S9†).[2] By using FORCs, we visualized the $H_c$ distributions in well-controlled NCMs, clarifying that the $H_c$ of the NCMs is dominated by a slight change in the phase segregation between a core/shell-like structure and a Janus-like structure.

## Results and discussion

### Synthesis of $L1_0$-FePd/α-Fe NCMs

To fabricate well-defined $L1_0$-FePd/α-Fe NCMs with monodisperse $L1_0$-FePd crystalline size, magnetic-domain shape of the NCMs and volume ratio of the $L1_0$-FePd/α-Fe phases, we performed the following step-by-step synthesis (Fig. 1a): (1) synthesis of monodisperse Pd nanocubes (NCs) (Fig. 1b and S1a–f†);[16,17] (2) homogeneous growth of $FeO_x$ shells on Pd NCs (Fig. 1c, S1g and Table S2†);[18] (3) reduction–diffusion of Pd/$FeO_x$ core/shell (Pd@$FeO_x$) NCs under the flow of 4% $H_2$ gas (Ar balance) (Fig. 1d, e and S5†).[4,5] This synthesis allowed us to finely tune the size of the Pd NCs, the thickness of the $FeO_x$ shell and the reduction–diffusion conditions, so we could precisely control the $L1_0$-FePd crystalline size and the volume fraction of the $L1_0$-FePd/α-Fe phases. The nanostructure of Pd@$FeO_x$ NCs also enabled the formation of a core/shell-like structure and a Janus-like structure under the reductive annealing (Fig. S4†). In addition, almost all particles were isolated after annealing because of the carbon shells formed from the organic ligands by Fe catalysis.[19] The phenomenon could be observed in the particles annealed under several conditions from high-resolution transition electron microscopy (HRTEM) (Fig. S3†).[19] We targeted a Pd grain size of 14–26 nm, which were estimated from TEM images, to facilitate the synthesis of the $L1_0$-FePd phase with a high ordering parameter.[20] We first focus on the samples synthesized by reductive annealing of Pd@$FeO_x$ NCs (from 19 nm Pd NCs) with Fe/Pd = 66/34 atomic% (at%) at 540 °C for 5, 10, 15, 20 and 25 h. X-ray diffraction (XRD) patterns show the formation of $L1_0$-FePd and α-Fe phases (Fig. S2b†). Thus, we formed magnets composed of $L1_0$-FePd and α-Fe phases with well-controlled nanostructural characteristics such as the $L1_0$-FePd crystalline size, the shape of the magnets and the α-Fe/$L1_0$-FePd volume ratio.

### Correlation of crystal and phase-segregation structures with $H_c$

Using vibrating sample magnetometer (VSM) on a series of $L1_0$-FePd/α-Fe NCMs, we showed that $H_c$ decreased monotonically with increasing annealing time (Fig. 2a). We attempted to explain this result by calculating the tetragonality—the ratio of lattice parameters ($c/a$)[9,21]—and the ordering parameter ($S$)[22,23] of the $L1_0$-FePd phase grains. Strangely, $S$ increased with annealing time (Fig. 2a) and $c/a$ decreased monotonically (Fig. S2c†), usually indicating that the $H_c$ of $L1_0$-FePd phase increased.[22] The crystalline size of the α-Fe phase grains also did not show a significant difference in the calculated values obtained by the Scherrer equation for the 110 diffraction peaks (Scherrer constant $K$ = 0.94) (Fig. S2†). Moreover, elemental maps measured with energy dispersive spectroscopy (EDS) did not show any differences in phase segregation among samples (Fig. 2b–d). These structural analyses could not explain the monotonic decrease in $H_c$ with annealing time.

Then, we used FORCs analysis on all the samples to clarify the nanostructure transformation that changed $H_c$ (Fig. 2e and f). To better compare the $H_c$ distributions, we integrated the height of the FORCs diagram ($\rho(H_c, H_u)$) with respect to the local interaction field ($H_u$). The obtained curve represents the fraction of hysteron for each $H_c$ (Fig. S9†). These curves were fitted with a Gaussian function, whose number was determined by kernel density estimation (Fig. S9†), and the fractions of these

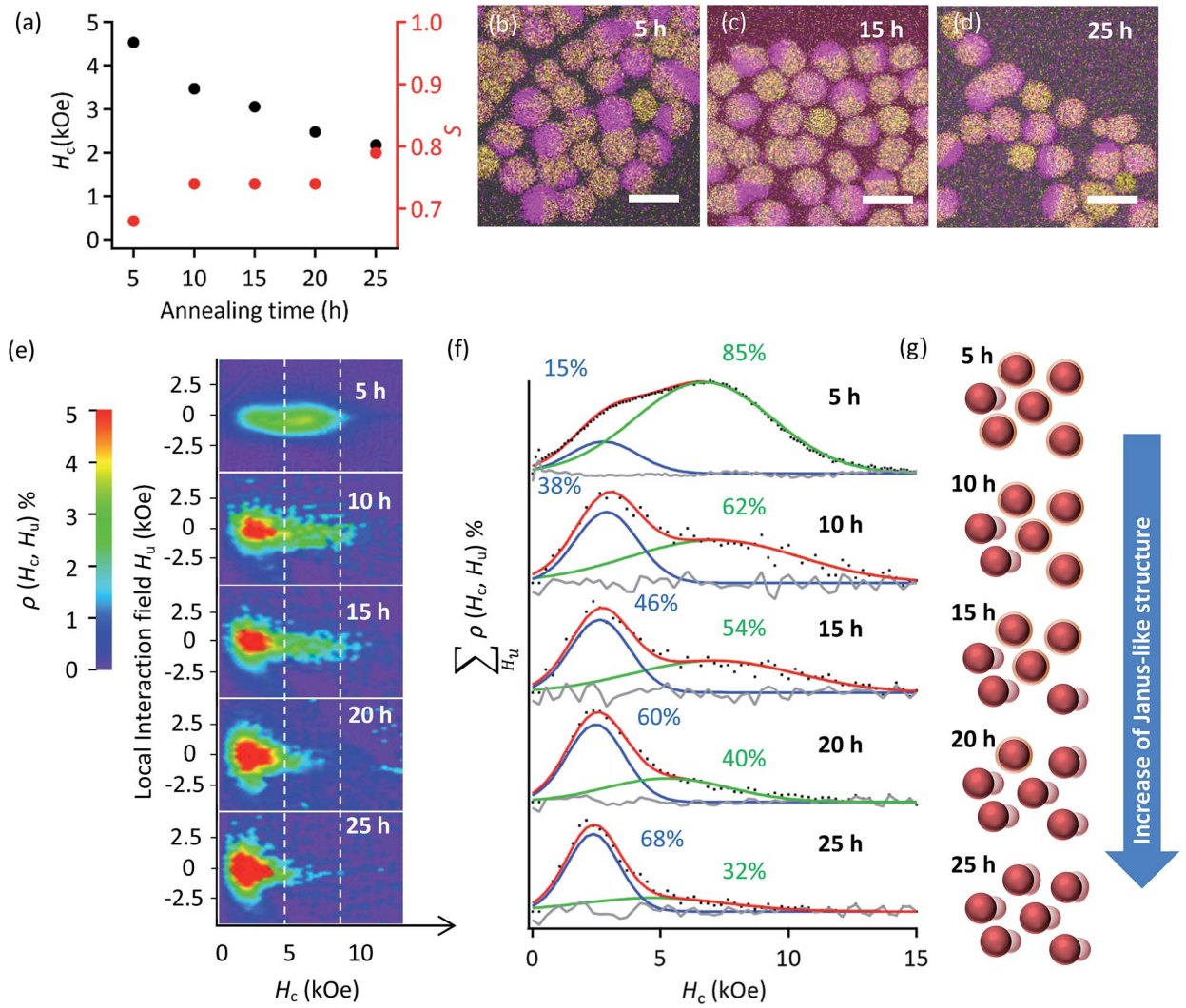


Fig. 2 (a) $H_c$ and $S$ values of the $L1_0$-FePd/α-Fe NCMs synthesized by reductive annealing of Pd@$FeO_x$ NCs with Fe/Pd = 66/34 at% synthesized from 19 nm Pd NCs annealed at 540 °C for various times. (b–d) Elemental maps of the NCMs obtained by reductive annealing for (b) 5 h, (c) 15 h and (d) 25 h (purple: Fe–K, yellow: Pd–L). Scale bars are 25 nm. (e) FORCs diagrams of the $L1_0$-FePd/α-Fe NCMs with Fe/Pd = 66/34 at% synthesized from 19 nm Pd NCs. $\rho(H_c, H_u)$ means the fraction of hysteron with a certain $H_c$ and a certain $H_u$. When $\rho(H_c, H_u)$ is over 5%, the colour becomes red. (f) $H_c$ distributions obtained by calculating the $\Sigma H_u \rho(H_c, H_u)$ of (e). The black dots are raw data, the red curves are the sums of the fitting curves by a Gaussian function, the blue and green curves are fitting curves and the grey curves are the differences between the raw data and fitting curves. (g) Schematics of the fraction change of the core/shell-like and Janus-like structures estimated by FORCs analysis of (f).

distributions were calculated from the integral of the fitting curves (Fig. 2f). Each FORCs diagram showed two $H_c$ distributions with quite high $H_c$ compared with that of the α-Fe soft phase ($H_c \ll 1$ kOe),[23,24] indicating that two types of NCMs formed.

The fraction of the low-$H_c$ distribution increasing with annealing time corresponds to a structural transformation from a core/shell-like structure to a Janus-like structure (Fig. S4†) or to the coalescence of α-Fe phase; the $L1_0$-FePd/α-Fe exchange coupling weakened because larger α-Fe phase grains formed during annealing (Fig. 2g).[4,25–28] In other words, the different thicknesses of α-Fe phase within and beyond the threshold determining 'efficient' or 'inefficient' exchange coupling in the $L1_0$-FePd/α-Fe NCMs helped to form the two types of NCMs. Thus, a visualization of the exchange coupling by FORCs analysis could reveal that a slight change, which was microscopically undetectable, in the phase-segregation structure or the α-Fe thickness dominated the $H_c$ of the NCMs.

## Optimization of nanostructure in $L1_0$-FePd/α-Fe NCMs for high performance

By controlling the crystalline size of the $L1_0$-FePd phase and the volume ratio of the $L1_0$-FePd/α-Fe phases (Fig. 1a), we fabricated NCMs with the highest performance reported in the Fe–Pd system. We synthesized NCMs as follows: (1) synthesis of Pd NCs with sizes of 14, 19, 23 and 26 nm; (2) homogeneous growth of $FeO_x$ shells on the Pd NCs with Fe/Pd molar ratios of approximately 62/38 and 66/34; (3) reductive annealing of

Pd@FeO$_x$ NCs under the conditions to produce NCMs with the highest $H_c$ (Fig. S5 and Table S4†).

Among all these NCMs, the NCMs formed from 19 nm Pd NCs had the highest $H_c$ regardless of Fe/Pd composition (Fig. S7a†). In the NCMs formed from 19 nm Pd NCs, we then controlled their $L1_0$-FePd/α-Fe volume fraction in the range of Fe/Pd = 53/47–75/25 at%, improving their $M_s$ and maximizing their energy product ($(BH)_{max}$) and $H_c/H_a$ ratio. These values became maximum ($(BH)_{max}$ = 17.5 MGOe and $H_c/H_a$ = 26.5%) at an Fe/Pd composition of 66/34 at% and decreased at >66/34 at% (Fig. 3a and b) due to the drastic decrease in $H_c$. These maximum values greatly exceeded the highest reported values ($(BH)_{max}$ = 10.3 MGOe and $H_c/H_a$ = 9%) in the Fe–Pd system.[4,5,25–28] Particularly, the $H_c/H_a$ value (26.5%) was also highest among all NCM powders to our knowledge, which indicates that the performance of $L1_0$-FePd/α-Fe NCMs was efficiently brought out, compared with other systems.[4–7,25–27]

To reveal which factor contributed to the high $H_c/H_a$ and $(BH)_{max}$, we again conducted FORCs analysis on these NCMs (Fig. 3c). The $H_c$ distributions revealed two types of exchange coupling derived from the Janus- and core/shell-like structures at Fe/Pd compositions of <66/34 at%. With more Fe, the lower $H_c$ distribution appeared in addition to the two types of NCMs, which was also derived from the NCMs with the Janus-like structure because this $H_c$ value is higher than that of α-Fe. On the other hand, the average $H_c$ of almost pure $L1_0$-FePd magnets (Fe/Pd = 53/47 at%) was lower than those of the NCMs with Fe/Pd molar ratios of 61/39 and 66/34. Then, the surface anisotropic constant ($K_s$) of these NCMs were compared, which strongly suggested that the low $K_s$ of pure $L1_0$-FePd magnets caused the lower $H_c$ *versus* those of $L1_0$-FePd/α-Fe NCMs (Fig. S8†). This result means that the soft magnetic phase in NCMs contributes not only to the increase of the $H_c$ with higher $K_s$ value, but also to the decrease of the $H_c$ due to the formation of Janus-like structure. Thus, the maximized $(BH)_{max}$ and $H_c/H_a$ at Fe/Pd = 66/34 at% came from the trade-off between the increase in $K_s$ and the decrease in the fraction of the core/shell-like structure.

### Clarification of the dominant factor determining the $H_c$ of $L1_0$-FePd/α-Fe NCMs

We estimated the change in exchange coupling between the $L1_0$-FePd and α-Fe phases by the phenomenological eqn (1) of the micromagnetics model (Fig. S10†):[29]

$$H_c = \alpha H_{aexp} - N_{eff} J_s, \quad (1)$$

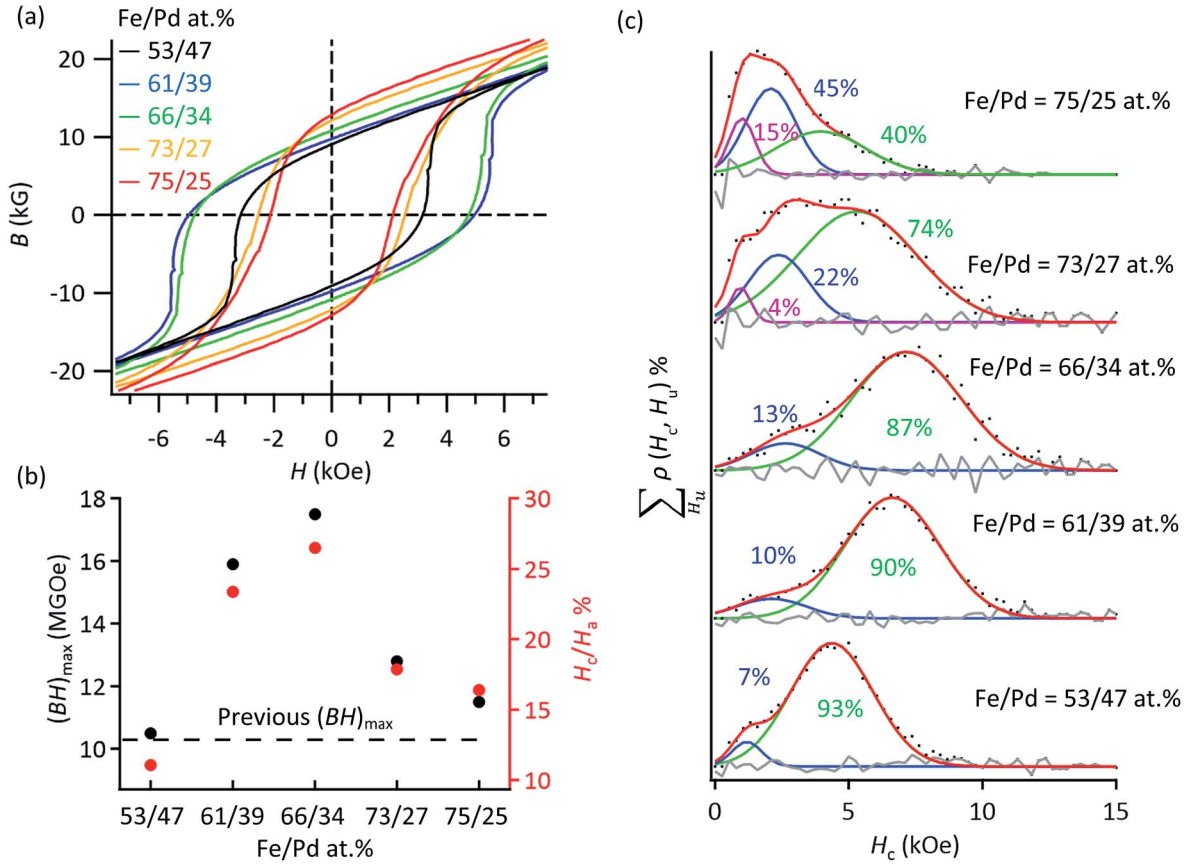


Fig. 3 (a) $B$–$H$ curves of the NCMs with Fe/Pd molar ratios of 53/47, 61/39, 66/34, 73/27 and 75/25 formed by reductive annealing at 590 °C for 3 h, at 570 °C for 10 h, at 560 °C for 3 h, at 540 °C for 3 h and at 540 °C for 3 h, respectively. The $B$ values were obtained from the corrected $M$–$H$ curve. (b) $(BH)_{max}$ and the $H_c/H_a$ values obtained from the $B$–$H$ curves. (c) $H_c$ distributions obtained by using the same method as in Fig. 2f. The cyan curves are also the $H_c$ distributions derived from the $L1_0$-FePd/α-Fe NCMs.

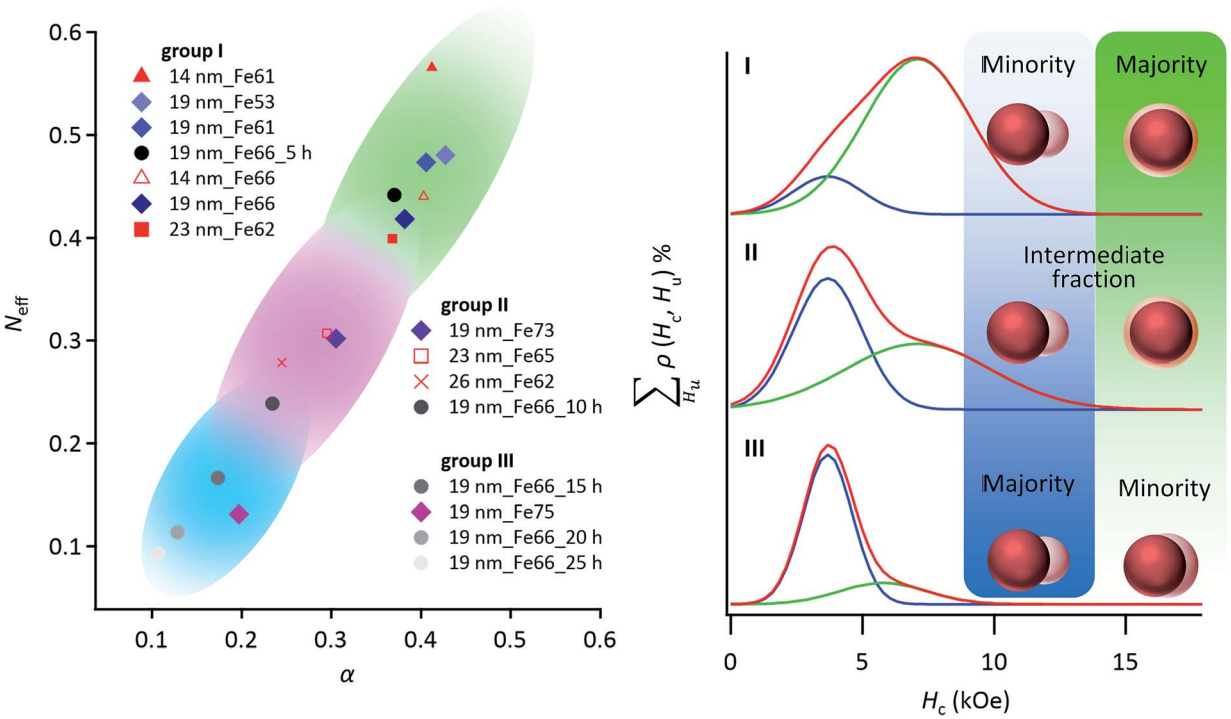


Fig. 4 According to a phenomenological eqn (1) of the micromagnetics model, both the effective demagnetization factor ($N_{eff}$) and effective micromagnetics constant ($\alpha$) were estimated for NCMs with different nanostructures. $\alpha$ and $N_{eff}$ strongly depend on the exchange coupling factor and the crystalline size of the $\alpha$-Fe soft magnetic phase,[32] respectively. The $\alpha$ and $N_{eff}$ values of the NCMs can be classified into groups I–III by using the $H_c$ distributions as follows: group I is the minor fraction of the Janus-like structure; group II is the intermediate fraction of the Janus-like structure; group III is the major fraction of the Janus-like structure. The sample name comprises the starting Pd NC size, followed by the Fe fraction, followed by the annealing time, if any.

where $\alpha$ is an effective microstructural parameter that varies from 0 to 1, which strongly depends on the exchange coupling factor;[30] $H_{aexp}$ is an anisotropy field of the NCMs, which is evaluated from the experimental results (Fig. S10†); $N_{eff}$ is an effective demagnetization factor, which usually decreases with an increasing amount of the soft magnetic phase, because the soft magnetic phase in NCMs can weaken the local stray field;[30] $J_s$ is the saturation magnetic polarization. Thus, $\alpha$ and $N_{eff}$ decreased as the fraction of the Janus-like structure increased. This behavior indicates that the structural change from core/shell- to Janus-like structures caused the decrease in exchange coupling between the $L1_0$-FePd and the $\alpha$-Fe phases and the increase in $\alpha$-Fe thickness, corresponding to the decrease in $\alpha$ and $N_{eff}$, respectively.

In fact, the micromagnetics model clearly explains the relationship between the fraction of the Janus-like structure and the $\alpha$ and $N_{eff}$ by classifying the $H_c$ distributions as follows (Fig. 4): (group I) low fraction of Janus-like structure, (group II) intermediate fraction of Janus-like structure and (group III) high fraction of Janus-like structure and transition from core/shell- to Janus-like structure. Thus, using FORCs analysis and the micromagnetics model, we showed that the $H_c$ of NCMs was dominated by the phase-segregation structure, because the strength of exchange coupling between the $L1_0$-FePd and the $\alpha$-Fe phases strongly depended on the thickness of the $\alpha$-Fe phase.

## Conclusions

The FORCs analysis results consistent with the micromagnetics model revealed that the Janus-like structure in NCMs caused the drastic decrease in $H_c$. In other words, the NCMs largely dominated by the core/shell-like structure provided the largest $(BH)_{max}$ (17.5 MGOe) in the Fe–Pd system and the highest $H_c/H_a$ value (26.5%) among all NCM powders,[4–7,25–28] because of the highly sensitive change of $H_c$ induced by the extremely slight transformation of phase-segregation structures. In our previous works,[4,5] we could not correctly evaluate the decrease in $H_c$, because it was quite difficult to discuss the boundary between 'efficient' and 'inefficient' exchange coupling between the hard and soft magnetic phases by using conventional methods such as TEM, XRD and EDS elemental mapping. FORCs analysis enables us to visually distinguish the two types of NCMs, revealing the dominant factor determining the $H_c$ of NCMs, that is, the phase-segregation fashion. These achievements can solve the mystery for the quite low $H_c$ of NCMs, compared with the theoretical $H_c$. We believe that the optimization of nanostructures by FORCs analysis can realize the creation of high-performance NCMs in not only Fe–Pd system but also other systems.

## Experimental procedure

### Chemicals

All reagents and solvents were commercially available. Sodium tetrapalladate(II) ($Na_2PdCl_4$, 98%), polyvinylpyrrolidone (PVP, $M_w \approx$ 55k), ascorbic acid (AA, 99+%), potassium bromide (KBr, ≥99%), oleylamine (OAm, 80–90%), 1-octadecene (ODE, 90%) and eicosane (99%) were purchased from Sigma-Aldrich. Iron pentacarbonyl ($Fe(CO)_5$, 95%) was purchased from Kanto Chemical Corporation. Oleic acid (OA, >85%) was purchased from Tokyo Chemical Industry. Ethanol, acetone, *n*-hexane and chloroform were purchased from Wako Pure Chemical Industries. All chemical reagents were used as received without further purification.

### Synthesis of Pd NCs

In typical synthesis of Pd NCs,[16] 270 mL of an aqueous solution of PVP (2.8 g) and AA (0.66 g) was stirred at 80 °C for 1 h. Then, an aqueous solution (30 mL) of $Na_2PdCl_4$ (1.5 g) and KBr (16 g) was rapidly injected into the above solution. The aqueous solution was stirred at 80 °C for 3 h and then cooled to room temperature. This process synthesized Pd NCs with an edge length of 15.4(±1.4) × 13.4(±1.1) nm (Fig. S1a†). To synthesize larger Pd NCs (Fig. S1b–d†), after an aqueous solution (250 mL) of $Na_2PdCl_4$ (1.5 g) and KBr (3.0 g) was stirred at 40 °C for 1 h, an aqueous solution of Pd seeds (*V* mL), an aqueous solution (25 mL) of PVP (2.8 g) and an aqueous solution (25 mL) of AA (1.8 g) were injected every 30 min at 40 °C (Fig. S1†). Here, the volume of the seed solution (*V* mL) was determined by the equation of the seeded-growth method:[17]

$$d = d_0((n_i + n_m)/n_m)^{1/3},$$

where $d$ is the average length of the final Pd NCs, $d_0$ is the average length of the Pd seeds and $n_i$ and $n_m$ are the quantities of ionic and metallic Pd in the reaction solution. The solution was stirred at 40 °C for 48 h, heated from 40 °C to 60 °C and stirred at 60 °C for 48 h. After the reaction, the reaction solution was cooled to room temperature, and the Pd NCs were collected by centrifugation with acetone and then purified with ethanol/acetone (1/4 vol%).

### Synthesis of Pd@$FeO_x$ NCs

Before $FeO_x$ growth on Pd NCs, we exchanged the organic ligand from PVP to OAm to disperse the Pd NCs in a low-polar solvent. The Pd NCs (0.50 mmol) protected by PVP were dispersed in the mixture of OAm (10 mL) and chloroform (20 mL) by sonication for 1 h, and then the solution was heated at 50 °C for 30 min. Then, the solution was cooled to room temperature, and the OAm-protected Pd NCs with sizes of 14 nm, 19 nm, 23 nm and 26 nm were collected with ethanol and purified *n* times ($n = 4$, 3, 2 and 1) with chloroform/ethanol (2/3 vol%), respectively. To cover the Pd NCs with $FeO_x$ shells, the OAm-protected Pd NCs (0.50 mmol), OAm (0.50 mL) and OA (0.91 mL) were dispersed in ODE (63 mL).[18] After the solution was stirred at 80 °C for 1 h under an $N_2$ atmosphere, $Fe(CO)_5$ ($x$ mmol) was injected into the solution (Table S2†) and the reaction temperature was increased in steps of 3 °C $min^{-1}$ from 80 °C to 180 °C. Finally, after the solution was stirred at 180 °C for 2 h and cooled to room temperature, Pd@$FeO_x$ NCs formed from the 14 nm, 19 nm, 23 nm and 26 nm Pd NCs were collected with ethanol and then purified three times with *n*-hexane/ethanol (3/1 vol%) including OAm (0.50 mL) and OA (0.50 mL).

### Synthesis of $L1_0$-FePd/α-Fe NCMs

After the Pd@$FeO_x$ NCs with sizes of 14 nm, 19 nm, 23 nm and 26 nm were washed *m* times ($m = 7$, 6, 5 and 4) with *n*-hexane, respectively, these NCs were dried in desiccator overnight. The $L1_0$-FePd/α-Fe NCMs were produced by reductive annealing—heating at 10 °C $min^{-1}$, holding at $T$ °C for $t$ h and cooling at 10 °C $min^{-1}$—of the Pd@$FeO_x$ NCs under an Ar + 4% $H_2$ atmosphere (see Fig. S5 and S6, and Table S4† for detailed conditions).

### Calculation of $S$ of the $L1_0$-FePd phase in $L1_0$-FePd/α-Fe NCMs

An $S$ of the $L1_0$-FePd phase was found with the following equation:[22]

$$S^2 = (I_{001}/I_{002})_{meas.}/(I_{001}/I_{002})_{calc.},$$

where $I_{001}$ and $I_{002}$ are the peak intensities of the *hkl* diffraction peaks in the $L1_0$-FePd phase, and $(I_{001}/I_{002})_{meas.}$ and $(I_{001}/I_{002})_{calc.}$ are the measured and calculated intensity ratios. We used 0.9852 (PDF#03-65-9971) as a calculated intensity ratio.

### Measurement of hysteresis loop at 300 K

The *M*–*H* curves were measured by a vibrating sample magnetometer (VSM, TOEI VSM-5) under a magnetic field ($H$) of −20 to 20 kOe, where the samples were prepared without aligning under the magnetic field. The samples were fixed with eicosane (melting point of 36.7 °C).

### Evaluation of temperature-dependent magnetic properties

The magnetic properties of the samples fixed by eicosane were measured on a PPMS-VS (Quantum Design EverCool II). The anisotropy constant ($K_u$) and anisotropy field ($H_{aexp}$) were calculated from *M*–*H* curve fits based on the following equation:[31]

$$M(H) = J_s(1 - 4K_u^2/15J_s^2H^2) + \chi H,$$

where $M(H)$ is the magnetization at $H$ and $\chi$ is the high-field susceptibility. $\alpha$ and $N_{eff}$ were determined using eqn (1) from a micromagnetics model, drawing a linear function from the points of $H_{aexp}$, $H_c$ and $J_s$ depending on temperature (Fig. S10†).

### FORCs analysis

The height of the FORCs diagram ($\rho$) was represented by the following equation:[14,15]

$$\rho(H_A, H_B) = -\partial^2 M(H_A, H_B)/2\partial H_A \partial H_B,$$

where $H_A$ and $H_B$ have the following relationship: a coercivity $H_c = -(H_A - H_B)/2$ and a local interaction field $H_u = (H_A + H_B)/2$. We applied a maximum $H$ of 50 kOe to produce magnetic saturation and the measurement pitch for $H_A$ and $H_B$ was 0.5 kOe within −20 kOe to 20 kOe of $H$ by using a superconducting quantum interference device (SQUID, Quantum Design MPMS XL) to measure the reversal magnetization in detail (Fig. S9†). The measurement temperature was 300 K. These samples were also fixed using eicosane.

#### Evaluation of $H_a$

$$H_a = 2(f_{volume}K_{uFePd} + (1 - f_{volume})K_{uFe})/(f_{volume}J_{sFePd} + (1 - f_{volume})J_{sFe}) = 2f_{volume}K_{uFePd}/(f_{volume}J_{sFePd} + (1 - f_{volume})J_{sFe})\ (K_{uFe} \ll K_{uFePd}),$$

where $f_{volume}$ is the volume fraction of the $L1_0$-FePd in NCMs, $K_{uFePd}$ (1.80 MJ m$^{-3}$) and $K_{uFe}$ (47.2 kJ m$^{-3}$) are the anisotropic constants of the $L1_0$-FePd and the α-Fe phases, respectively and $J_{sFePd}$ (13.8 kG) and $J_{sFe}$ (21.5 kG) are the saturation magnetizations of the $L1_0$-FePd and the α-Fe phases, respectively.[3,5,24]

#### Evaluation of $(BH)_{max}$

To calculate the $(BH)_{max}$, we measured the density of the NCMs and the demagnetization field of the magnets by using VSM.

(i) Volume ratio of $L1_0$-FePd/α-Fe phases

The volume fraction is calculated from the Fe/Pd at% as follows:

$$L1_0\text{-FePd cm}^3\text{: } f_{at}(M_{Fe} + M_{Pd})/d_{FePd},$$

$$\alpha\text{-Fe cm}^3\text{: } (1 - 2f_{at})M_{Fe}/d_{Fe},$$

where $f_{at}$ is the fraction of Pd atoms in the $L1_0$-FePd/α-Fe NCMs measured by XRF, $M_{Fe}$ and $M_{Pd}$ are the atomic weights of Fe and Pd atoms, respectively and $d_{FePd}$ (9.75 g cm$^{-3}$) and $d_{Fe}$ (7.86 g cm$^{-3}$) are the densities of the $L1_0$-FePd and α-Fe phases, respectively.[4]

(ii) Density of $L1_0$-FePd/α-Fe NCMs

From (i), we can estimate the density of the NCMs ($d_{NCMs}$) as follows:

$$d_{NCMs} = (f_{at}(M_{Fe} + M_{Pd}) + (1 - 2f_{at})M_{Fe})/(f_{at}(M_{Fe} + M_{Pd})/d_{FePd} + (1 - 2f_{at})M_{Fe}/d_{Fe}).$$

(iii) Conversion of magnetization unit from [emu g$^{-1}$] to [G]

We converted the magnetization unit from [emu g$^{-1}$] to [G] as follows:

$$J = Md_{NCMs}4\pi,$$

where $J$ is the magnetic polarization and $M$ is the magnetization.

(iv) Correction of magnetic field

To estimate the magnetic flux density ($B$), $H$ should be corrected by removing the demagnetization field ($N_zJ$) as follows:

$$H_{correct} = H - N_zJ,$$

$$N_z = 1/(1 + c/a^2(a(a + c))^{1/2}),$$

where $H$ and $H_{correct}$ are the magnetic fields before and after correction, $N_z$ is a demagnetization factor of magnets along the $z$ axis, and $a$ and $c$ are the radius and height of the cylinder, respectively, during the VSM measurement.[32]

(v) Evaluation of $(BH)_{max}$

$$B = J + H_{correct}.$$

Finally, the $(BH)_{max}$ values are obtained from $B \times H_{correct}$ in the second quadrants of the $B$–$H$ curves.

#### TEM observation

The Pd NCs and Pd@$FeO_x$ NCs were dispersed in ethanol and chloroform, respectively and then dropped on amorphous carbon-coated copper grids with a carbon thickness of about 30 nm. TEM samples for the $L1_0$-FePd/α-Fe NCMs were prepared by annealing the Pd@$FeO_x$ NCs on TEM grids. TEM images were recorded on a JEM1011 (JEOL) at an acceleration voltage of 100 kV.

#### Powder XRD measurement

The XRD patterns were recorded on a PANalytical X'Pert Pro MPD diffractometer with Cu Kα radiation ($\lambda = 1.542$ Å) at 45 kV and 40 mA.

#### Evaluation of the composition of $L1_0$-FePd/α-Fe NCMs

The Fe/Pd molar ratios of the NCs and NCMs were measured by X-ray fluorescence (XRF) spectroscopy (JEOL JSX-3202C). The $L1_0$-FePd/α-Fe volume ratios were calculated on the hypothesis that the Pd phase grains were completely converted into the $L1_0$-FePd phase grains (Table S1†).

#### EDS elemental maps by HAADF-STEM and HRTEM

The TEM samples of the $L1_0$-FePd/α-Fe NCMs were prepared by annealing the Pd@$FeO_x$ NCs on amorphous carbon-coated copper grids with a carbon thickness of about 5 nm. EDS maps by HAADF-STEM and HRTEM were performed on a JEM-ARM200F at an acceleration voltage of 200 kV.

## Conflicts of interest

There are no conflicts to declare.

## Acknowledgements

This work was supported by The Ministry of Education, Culture, Sports, Science and Technology (MEXT)/Japan Society for the Promotion of Science (JSPS) KAKENHI for Scientific Research B (Grant No. JP16H03826 (T. T.)) and for JSPS Research Fellowship (Grant No. JP18J15062 (K. M.)). This research was also supported by the 'Development of magnetic material technology for

high-efficiency motors' program commissioned by the New Energy and Industrial Technology Development Organization (NEDO) and the Elements Strategy Initiative Center for Magnetic Materials (ESICMM) project from MEXT.

## References

1 N. Jones, *Nature*, 2011, **472**, 22–23.
2 J. P. Liu, E. Fullerton, O. Gutfleisch and D. J. Sellmyer, *Nanoscale Magnetic Materials and Applications*, ed. J. P. Liu, Springer, Berlin, 2009, pp. 309–335.
3 E. F. Kneller and R. Hawig, *IEEE Trans. Magn.*, 1991, **27**, 3588–3600.
4 N. Sakuma, T. Ohshima, T. Shoji, Y. Suzuki, R. Sato, A. Wachi, A. Kato, Y. Kawai, A. Manabe and T. Teranishi, *ACS Nano*, 2011, **5**, 2806–2813.
5 T. Teranishi, A. Wachi, M. Kanehara, T. Shoji, N. Sakuma and M. Nakaya, *J. Am. Chem. Soc.*, 2008, **130**, 4210–4211.
6 H. Zeng, J. Li, J. P. Liu, Z. L. Wang and S. Sun, *Nature*, 2002, **28**, 395–398.
7 F. Liu, J. Zhu, W. Yang, Y. Dong, Y. Hou, C. Zhang, H. Yin and S. Sun, *Angew. Chem., Int. Ed.*, 2014, **53**, 2176–2180.
8 Y. Tamada, S. Yamamoto, M. Takano, S. Nasu and T. Ono, *Appl. Phys. Lett.*, 2007, **90**, 162509.
9 T. Burkert, L. Nordström, O. Eriksson and O. Heinonen, *Phys. Rev. Lett.*, 2004, **93**, 027203.
10 Q. Song and Z. J. Zhang, *J. Am. Chem. Soc.*, 2004, **126**, 6164–6168.
11 A. Ramazani, M. A. Kashi and A. H. Montazer, *J. Appl. Phys.*, 2014, **115**, 113902.
12 V. Nandwana, G. S. Chaubey, K. Yano, C.-B. Rong and J. P. Liu, *J. Appl. Phys.*, 2009, **105**, 014303.
13 T. B. Massalski, H. Okamoto, P. R. Subramanian and L. Kacprzak, *Binary Alloy Phase Diagrams*, ed. T. B. Massalski, ASM intl., Almere, 2nd edn, 1990, vol. 2, pp. 1749–1751.
14 I. D. Mayergoyz, *J. Appl. Phys.*, 1985, **57**, 3803.
15 C.-I. Dobrotă and A. Stancu, *J. Appl. Phys.*, 2013, **113**, 043928.
16 T. T. Trinh, R. Sato, M. Sakamoto, Y. Fujiyoshi, M. Haruta, H. Kurata and T. Teranishi, *Nanoscale*, 2015, **7**, 12435–12444.
17 R. Sato, M. Kanehara and T. Teranishi, *Small*, 2011, **7**, 469–473.
18 H. Kura, M. Takahashi and T. Ogawa, *J. Phys. Chem. C*, 2010, **114**, 5835–5838.
19 Z. He, J.-L. Maurice, A. Gohier, C. S. Lee, D. Pribat and C. S. Cojocaru, *Chem. Mater.*, 2011, **23**, 5379–5387.
20 K. Sato, *Nat. Mater.*, 2009, **8**, 924–925.
21 T. J. Klemmer, N. Shukla, C. Liu, X. W. Wu, E. B. Svedberg, O. Mryasov, R. W. Chantrell, D. Weller, M. Tanase and D. E. Laughlin, *Appl. Phys. Lett.*, 2002, **81**, 2220–2222.
22 S. Okamoto, N. Kikuchi, O. Kitakami, T. Miyazaki, Y. Shimada and K. Fukamichi, *Phys. Rev. B: Condens. Matter Mater. Phys.*, 2002, **66**, 024413.
23 H. Gengnagel and U. Hofmann, *Phys. Status Solidi*, 1968, **29**, 91–97.
24 M. W. Grinstaff, M. B. Salamon and K. S. Suslick, *Phys. Rev. B: Condens. Matter Mater. Phys.*, 1993, **48**, 269–274.
25 Y. Yu, K. Sun, Y. Tian, X.-Z. Li, M. J. Kramer, D. J. Sellmyer, J. E. Shield and S. Sun, *Nano Lett.*, 2013, **13**, 4975–4979.
26 A. Kirkeminde and S. Ren, *Nano Lett.*, 2014, **14**, 4493–4498.
27 F. Liu, Y. Dong, W. Yang, J. Yu, Z. Xu and Y. Hou, *Chem.–Eur. J.*, 2014, **20**, 15197–15202.
28 S. H. Liu, C. C. Chen, S. N. Hsiao, S. K. Chen, Y. C. Chang, S. H. Su and K. F. Chiu, *Appl. Phys. A*, 2015, **119**, 623–627.
29 X. C. Kou, H. Kronműller, D. Givord and M. F. Rossignol, *Phys. Rev. B: Condens. Matter Mater. Phys.*, 1994, **50**, 3849–3860.
30 J. Bauer, M. Seeger, A. Zern and H. Kronműller, *J. Appl. Phys.*, 1996, **80**, 1667–1673.
31 G. Hadjipanayis, D. J. Sellmyer and B. Brandt, *Phys. Rev. B: Condens. Matter Mater. Phys.*, 1981, **23**, 3349–3354.
32 R. J. Parker, *Advances in Permanent Magnetism*, Wiley, New York, 1990.